



Site occupancy of Fe²⁺, Fe³⁺ and Ti⁴⁺ in titanomagnetite determined by valence-difference contrast in synchrotron X-ray resonant scattering

Maki Okube,^{a*} Taro Oshiumi,^a Toshiro Nagase,^b Ritsuro Miyawaki,^c
 Akira Yoshiasa,^d Satoshi Sasaki^{e,f*} and Kazumasa Sugiyama^a

Received 6 March 2018

Accepted 2 October 2018

Edited by V. Favre-Nicolin, CEA and
 Université Joseph Fourier, France

Keywords: resonant scattering; anomalous scattering; valence-difference contrast; titanomagnetite; single-crystal X-ray diffraction; Fe K absorption edge.

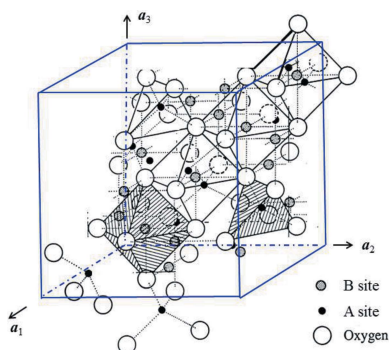
^aInstitute for Material Research, Tohoku University, Sendai 980-8577, Japan, ^bTohoku University Museum, Tohoku University, Sendai 980-8578, Japan, ^cDepartment of Geology and Paleontology, National Museum of Nature and Science, Tsukuba 305-0005, Japan, ^dGraduate School of Science and Technology, Kumamoto University, Kumamoto 860-8555, Japan, ^eMaterials and Structures Laboratory, Tokyo Institute of Technology, Yokohama 226-8503, Japan, and ^fInstitute of Materials Structure Science, High Energy Accelerator Research Organization, Tsukuba 305-0801, Japan.
 *Correspondence e-mail: makisan@imr.tohoku.ac.jp, sasaki@materia.titech.ac.jp

A synchrotron X-ray diffraction study of a single crystal of titanomagnetite shows that the cation distribution of Fe²⁺, Fe³⁺ and Ti⁴⁺ is of the inverse-spinel type. The valence-difference contrast (VDC) method of resonant scattering was applied at a wavelength of $\lambda = 1.7441 \text{ \AA}$ ($E = 7.1085 \text{ keV}$) within the pre-edge of the Fe K absorption spectrum, utilizing the large difference in the real part of anomalous scattering factors, between -7.45 and -6.50 , for Fe²⁺ and Fe³⁺, respectively. The most plausible atomic arrangement in Ti_{0.31}Fe_{2.69}O₄ obtained from our analysis is $[\text{Fe}_{1.00}^{3+}]^A[\text{Fe}_{0.38}^{3+}\text{Fe}_{1.31}^{2+}\text{Ti}_{0.31}^{4+}]^B\text{O}_4$, where *A* and *B* in an AB₂O₄-type structure correspond to the tetrahedral and octahedral sites, respectively. This result suggests that titanomagnetite has the complete inverse-spinel structure continuously from the end-member of magnetite, even in the case of relatively high Ti content. The physical properties may be described by the Néel model, which claims that Fe³⁺ preferentially occupies the tetrahedral site, within a Ti-poor half-region of the solid solution. Based on the ordering scheme the magnetic structure of titanomagnetite is considered to be analogous to that of magnetite. The combination of circularly polarized X-rays and a horizontal-type four-circle diffractometer used in this VDC technique has the advantage of increasing the experimental accuracy and freedom with the simultaneous reduction of experimental noise.

1. Introduction

Knowledge of the valence of cations in crystalline solids is important because it helps to understand the relationship between crystal structure and physical properties in materials science, chemistry and mineralogy. In terms of crystal-structure analysis in the high-resolution base, the use of synchrotron X-rays is of great advantage to achieve high accuracy of measurements and to collect more information on Bragg reflections. The continuous spectrum of synchrotron radiation is essential in selecting the wavelengths needed for the valence analysis. The combination of spectroscopy and X-ray diffraction creates plenty of room for the development of experimental approaches to improve accuracy in synchrotron radiation research. In this study, the synchrotron X-ray data have been analyzed to examine the valence of Fe ions in titanomagnetite and also to aim to improve the experimental and analytical accuracy.

The majority of magnetic minerals present on the Earth are iron-containing compounds. Knowledge of the magnetic properties and magnetic crystal structures of such minerals is



important, particularly for paleomagnetism studies, as magnetic minerals can be used as a tracer for the past magnetic fields of the Earth. Titanomagnetite $\text{Ti}_x\text{Fe}_{3-x}\text{O}_4$ is one of the major magnetic sources in rock-forming minerals. Titanomagnetite is a member of the cubic spinel family (Nishikawa, 1915; Bragg, 1915). The crystal structure can be described as cubic close packing of oxygen atoms with two cation sites known as the tetrahedral *A* ($8a$ Wyckoff position, site symmetry $\bar{4}3m$) and octahedral *B* sites ($16d$, $\bar{3}m$) (Fig. 1). In titanomagnetite, the replacement of Fe^{3+} by Ti^{4+} yields an increase in Fe^{2+} to maintain charge neutrality, and the partition of cations between the *A* or *B* sites needs to be fully understood, because an increase in Fe^{2+} in the tetrahedral *A* site gives rise to magnetostriction and a high coercive force, affecting the paleomagnetic properties of the Earth. The magnetic and electronic properties depend strongly on the cation distribution between these sites. Two extreme structures have been defined: the normal spinel, $[\text{Y}^{\text{A}}[\text{ZZ}]^{\text{B}}\text{O}_4]$, as represented by Mn–Zn ferrite (Okita *et al.*, 1998), and the inverse spinel, $[\text{Z}]^{\text{A}}[\text{YZ}]^{\text{B}}\text{O}_4$, as represented by Ni ferrite (Tsukimura *et al.*, 1997). Titanomagnetite is a solid solution lying between magnetite (Fe_3O_4) and ulvöspinel (TiFe_2O_4). The purpose of this study was to determine the cation distribution in the intermediate compounds and to resolve some of the ambiguities in the discussion of the physical properties of titanomagnetite, such as its magnetic saturation moment.

Magnetite is one of the end-member compositions that have the inverse spinel structure of $[\text{Fe}^{3+}]^{\text{A}}[\text{Fe}^{2+}\text{Fe}^{3+}]^{\text{B}}\text{O}_4$, where one-half of Fe^{3+} per formula unit occupies the tetrahedral site while Fe^{2+} and the remaining half of Fe^{3+} occupy the octahedral site in a 1:1 ratio (Verwey & de Boer, 1936). Various physical properties of magnetite, such as metallic behavior and magnetization, depend on the cation distribution of Fe^{2+} and Fe^{3+} between these two sites. The high electronic conductivity at room temperature is related to electron hopping due to an averaged distribution of Fe^{2+} and Fe^{3+} in the crystal-

lographically identical *B* site. High-spin Fe cations in this inverse-spinel arrangement are distributed with antiparallel spin between the *A* and *B* sites. Fe^{2+} and Fe^{3+} have magnetic moments of $4\mu_{\text{B}}$ and $5\mu_{\text{B}}$, respectively. The arrangement having Fe^{3+} at the *A* site and a pair of Fe^{2+} and Fe^{3+} coupled antiparallel at the *B* site gives a net $4\mu_{\text{B}}$ magnetization per formula unit. At lower temperatures the conductivity decreases with magnetic anisotropy, and at the Verwey transition temperature ($T_{\text{V}} \simeq 123$ K) a metal–insulator transition occurs with charge ordering with partial charge disproportionation in a lower symmetry (Verwey & Haayman, 1941; Verwey *et al.*, 1947; Samuelsen *et al.*, 1968; Yamada *et al.*, 1968; Iizumi *et al.*, 1982; Toyoda *et al.*, 1999). The other end-member is ulvöspinel, which has an inverse-spinel structure identical to $[\text{Fe}^{2+}]^{\text{A}}[\text{Fe}^{2+}\text{Ti}^{4+}]^{\text{B}}\text{O}_4$ (Barth & Posnjak, 1932). Magnetization measurements suggest spontaneous magnetization below the Néel temperature ($T_{\text{N}} \simeq 140$ K), with a maximum magnetization of $0.36\mu_{\text{B}}$ per formula unit and a small distortion below $T \simeq 100$ K (Ishikawa, 1967). The temperature dependence of the Mössbauer spectra suggests that two subsets of the spin align antiparallel between Fe^{2+} ions in the *A* and *B* sites (Ôno *et al.*, 1968). The site preference in titanomagnetite is still in dispute because of the difficulty in distinguishing between Fe^{2+} and Fe^{3+} in the three-component system, including Ti^{4+} , in crystal-structure analyses. Accurate determination of the site occupancy has depended on the accuracy of data collection using the anomalous scattering effect at the Fe *K* absorption edge with synchrotron radiation X-rays. The other limiting factor is the existence of a miscibility gap (solvus) in the middle part of titanomagnetite solid solutions, with an intergrowth texture of magnetite-rich crystals and ulvöspinel-rich exsolution lamellae (Lilova *et al.*, 2012).

The site preference of Ti^{4+} in titanomagnetite can be investigated using conventional crystal-structure determination methods such as X-ray or neutron diffraction, and it has been concluded that Ti^{4+} exclusively occupies the octahedral *B* site (Blasse, 1964; Forster & Hall, 1965; Fujino, 1974; Wechsler *et al.*, 1984). Before the introduction of the anomalous scattering technique, the estimation of the site occupancy between Fe^{2+} and Fe^{3+} was based on information from measurements of magnetic saturation moments. The cation distribution has therefore remained enigmatic because the presence of impurity phases leads to an uncertain relationship between magnetism and cation distribution. Three models have been proposed for titanomagnetite. One is a simple substitution model in which Fe^{3+} is concentrated equally between the *A* and *B* sites, and one Fe^{2+} per formula unit constantly occupies the *B* site (Akimoto model; Akimoto, 1954); the statistically random distribution may lead to higher configurational entropy at higher temperatures. The second model is based on a site preference in which Fe^{3+} exclusively occupies the tetrahedral site for $x \leq 0.5$, while Fe^{2+} always prefers octahedral coordination (Néel model; Néel, 1955; Chevallier *et al.*, 1955). This model produces a discontinuity at $x = 0.5$ for the chemical trend in saturation magnetization. According to the third model, additional Fe^{2+} ions enter tetrahedral sites in the range $0.2 \leq x \leq 0.8$ (O'Reilly–Banerjee model; O'Reilly &

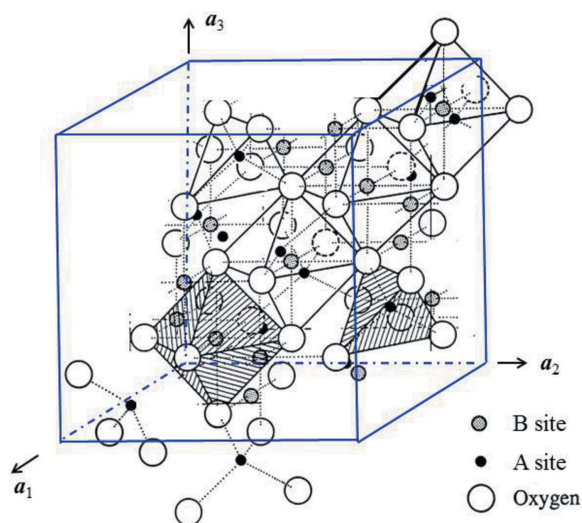


Figure 1
Crystal structure of titanomagnetite, showing *A* and *B* sites and oxygen atoms.

Banerjee, 1965); in this model, the saturation magnetization is higher than in the Néel model, but lower than in the Akimoto model. The saturation moments of synthetic titanomagnetite samples fall in the intermediate position between the two models (Akimoto *et al.*, 1957). In addition, some complex models for cation distribution have been proposed to provide estimates of the cation distribution based on magnetic properties or spectroscopic measurements (Kakol *et al.*, 1991; Hamdeh *et al.*, 1999; Bosi *et al.*, 2009). An approach from X-ray magnetic circular dichroism (XMCD) has been reported for measurements of titanomagnetite at the Fe $L_{2,3}$ -edge. These are element specific but are based on a powder-sample technique, so any discussion of the interpretation of the origin of the spectra can be only qualitative (Pearce *et al.*, 2010). Analysis of saturation magnetization data yields the further difficulty that the cation distribution is temperature dependent in the titanomagnetite solid solution series (Stephenson, 1969; Bleil, 1971, 1976), which is common in some spinel ferrites such as Mn ferrite (Ohara *et al.*, 2000) and Mn–Zn ferrite (Sakurai *et al.*, 2008).

The most suitable method for determining the cation distribution between Fe^{2+} and Fe^{3+} is resonant scattering (or anomalous scattering) with strong valence contrast. Larger differences in the atomic scattering factor f lead to greater differences in X-ray scattering power. A larger difference between $f(\text{Fe}^{2+})$ and $f(\text{Fe}^{3+})$ contributes to the crystal structure factor, providing high accuracy in determining the cation distribution with small experimental error. The first synchrotron radiation experiment for site-occupancy determination was conducted in a study of $(\text{Co},\text{Fe})_3\text{O}_4$, where this method has sufficient scattering power to distinguish adjacent elements in the periodic table such as Co and Fe (Yakel, 1980). Even if the same target atom has a different valence or oxidation state, the treatment of discrimination in f is the same for different anomalous scattering factors. The valence difference of ions appears in chemical shifts of X-ray absorption spectrum. The difference appears in anomalous scattering factors since the anomalous dispersion is closely related to resonant absorption phenomena. The anomalous scattering factors can be calculated from absorption spectra by applying the dispersion relation described by Kramers and Krönig (*e.g.* Sreaton, 1960). In the vicinity of X-ray absorption thresholds, the X-ray anomalous scattering factors are sufficient to distinguish the oxidation state of ions. The use of differences in anomalous scattering factors for ions with different valence has been proposed as a valence-difference contrast (VDC) method (Wilkinson & Cheetham, 1992; Sasaki, 1995; Sasaki *et al.*, 1998). Associated with a chemical shift of several eV at wavelengths close to the Fe K absorption edge, the VDC method can detect the anisotropic intensity distribution of X-ray diffuse scattering related to the valence fluctuation of Fe ions in magnetite (Toyoda *et al.*, 1997). Similar attempts to use the VDC method have been reported for Eu_3S_4 (Ohara *et al.*, 2004) and Yb_4As_3 (Nakao *et al.*, 2006). Some applications of the resonant diffraction studies have been reported on valence and charge ordering with similar crystal structures (*e.g.* Grenier *et al.*, 2002; Palancher *et al.*,

2005; Beale *et al.*, 2012; Subías *et al.*, 2012; Okube & Sasaki, 2014).

Thus, analysis of the site occupancy of titanomagnetite is now feasible with sufficient accuracy using X-ray resonant scattering. In this study, the site occupancies of Ti, Fe^{2+} and Fe^{3+} were simultaneously determined for the A and B sites of the spinel structure using the VDC method of single-crystal X-ray diffraction at the Fe K pre-edge.

2. Experimental

The sample was a single crystal of natural titanomagnetite from the Kabasawa Mine, Miyagi Prefecture, Japan, which was provided by the National Museum of Nature and Science (sample number 19373). Chemical analyses using an electron probe microanalyzer showed that the titanomagnetite had the chemical formula $\text{Ti}_{0.31}\text{Fe}_{2.69}\text{O}_4$. The space group and cell dimensions were $Fd\bar{3}m$ and $a = 8.414(2)$ Å, respectively, determined using a conventional AFC-7 Rigaku four-circle diffractometer with Mo $K\alpha$ radiation.

Synchrotron experiments were performed at beamline BL-6C of the Photon Factory with a wavelength of $\lambda = 1.7441$ Å ($E = 7.1085$ keV) at the Fe K pre-edge selected using an Si(111) double-crystal monochromator. Integrated intensity measurements were conducted with a Rigaku AFC-5u four-circle diffractometer, which is ordinarily and regularly installed in the BL-6C experimental hutch. Since the diffractometer is equipped with a scintillation detector scanning in the horizontal direction, right-handed circular polarization (helicity = +1) was used so that an incident intensity does not affect the intensive reduction of intensity like the linear polarization effect. Then, the polarization factor P for circular polarization is given by $(1 + \cos^2 2\theta)/2$, which is similar to the case of an unpolarized X-ray beam. The incident beam was guided into a synthetic (001) diamond with a thickness of 0.492 mm acting as a phase retarder to produce circularly polarized X-rays. The diamond crystal was set near the 111 Bragg condition in the asymmetric Laue case, with the scattering plane inclined by 45° from the vertical plane (Hirano *et al.*, 1991).

A single crystal of $50\ \mu\text{m} \times 50\ \mu\text{m} \times 70\ \mu\text{m}$ was mounted onto a glass fiber for the X-ray diffraction study. Integrated intensity data were collected in the ω - 2θ scan mode of the AFC-5u, with the ω -scan speed and width set at $0.5^\circ\ \text{min}^{-1}$ and 0.8° , respectively, selecting within the ranges $2\theta \leq 130^\circ$ ($\sin\theta/\lambda \leq 0.520$), and $-8 \leq h \leq 8$, $-8 \leq k \leq 8$ and $-8 \leq l \leq 8$. As the top-up mode was not available for our experiments at the Photon Factory storage ring, the intensity data for each reflection were corrected using three standard reflections of $40\bar{4}$, 400 and $\bar{1}3\bar{1}$ to compensate for incident beam intensity decay. Lorentz and absorption effects were corrected using a linear absorption coefficient of $\mu = 369.5\ \text{cm}^{-1}$ ($\lambda = 1.7441$ Å). The transmission factors ranged from 0.17 to 0.25. Of 687 reflections measured ($R_{\text{int}} = 0.04$), 432 reflections $> 3\sigma_F$ were used for refinements after cubic averaging. The crystal structure was refined by full-matrix least-squares minimization of the residual factor, $\sum w_i(|F_{\text{obs}}| - |F_{\text{calc}}|)^2$, using the program

RADY (Sasaki, 1987), which allows occupancy refinements to vary parameters under constraints in chemical composition. An isotropic extinction correction was applied to express the observed intensity by the kinematical diffraction theory (Becker & Coppens, 1974). The positional parameter of oxygen and anisotropic temperature factors for all atoms were simultaneously refined with $R = 0.051$, $wR = 0.049$ ($w = 1/\sigma_F^2$) for the Fe K data set. The u parameter was determined to be 0.2539 (11). Thermal parameters β_{11} , β_{12} and B_{eq} were 0.0023 (4), 0 and 0.66 (3) for the A site, 0.0022 (5), -0.0001 (3) and 0.61 (5) for the B site and 0.0012 (6), -0.0001 (5) and 0.35 (6) for the oxygen site, respectively, where B_{eq} is an equivalent isotropic temperature factor and the standard deviation is given for the last digit in parentheses. The maximum ratio between the change and error parameters, Δ/σ , was 0.56×10^{-5} for the atomic coordinate x of the oxygen atoms.

The absorption measurements were conducted at BL-6C with a beam of dimensions 1 mm \times 2 mm and two ionization chambers with N_2 (monitor) and 85% N_2 + 15% Ar gas. The thickness of the samples was adjusted for suitable absorption. Powder samples of FeO, Fe_2O_3 and magnetite (High Purity Chemical Laboratory Co. Ltd) were used as received for the absorption measurements. Energy calibration on the Fe K -edge was conducted for iron metal foil of 5 μm thickness with the inflection point of the shoulder structure in the absorption spectrum, which is assigned as $E = 7.1120$ keV. The conversion from X-ray energy in keV to wavelength in \AA was conducted using a factor of 12.398 (Thompson *et al.*, 2001). All experiments were made at room temperature.

3. Absorption spectra and chemical shift

To conduct a preliminary examination of the valence state of Fe ions in titanomagnetite, X-ray absorption near-edge structure (XANES) spectra were measured at the Fe K absorption edges at room temperature. Fig. 2 shows the XANES spectra of titanomagnetite, iron metal foil, FeO (NaCl structure), Fe_3O_4 (spinel structure) and Fe_2O_3 (corundum structure). A chemical shift of about 6.1 eV clearly exists between Fe^{2+} in FeO and Fe^{3+} in Fe_2O_3 over a threshold region, where the Fe ions in FeO and Fe_2O_3 have sixfold coordination with oxygen atoms in a regular FeO_6 octahedron. The chemical shift was about 1 eV larger than in our previous report (Sasaki, 1995). It seems that the powder sample used for that earlier study was slightly oxidized [*e.g.* Fig. 1 of Sasaki (1995), Fig. 3 of Sakurai *et al.* (2008)]. The photon energies at specific XANES positions and the values of chemical shifts are summarized for some iron compounds in Table 1. Compared with the 50% absorption data from XANES spectra, the threshold energy of titanomagnetite falls between the divalent and trivalent states, 2.4 eV higher than that of FeO, 3.7 eV lower than that of Fe_2O_3 , and 2.6 eV lower than that of magnetite Fe_3O_4 . This indicates that both Fe^{2+} and Fe^{3+} exist in titanomagnetite and that the Fe^{2+} content of titanomagnetite is greater than that of magnetite. The pre-edge peaks of FeO, titanomagnetite, Fe_3O_4 and Fe_2O_3 are arranged with

Table 1

Photon energy and chemical shift of XANES spectra for iron compounds at the Fe K absorption edge.

The inflection point of the shoulder structure of iron metal foil is assigned as the Fe K -edge ($E = 7.1120$ keV). The energy resolution at the Fe K -edge is about 0.9 eV for the Si(111) monochromator.

Sample	Photon energy			
	Pre-edge peak	20% absorption	50% absorption	Main-edge peak
Iron metal foil (keV)		7.1076	7.1148	7.1263
FeO (Fe^{2+}) (keV)	7.1076	7.1115	7.1144	7.1235
Chemical shift† (eV)		3.8	-0.4	-2.8
$\text{Ti}_{0.31}\text{Fe}_{2.69}\text{O}_4$ (keV)	7.1083	7.1144	7.1168	7.1262
Chemical shift† (eV)		6.7	2.0	-0.1
Fe_3O_4 (keV)	7.1096	7.1158	7.1194	7.1266
Chemical shift† (eV)		8.1	4.6	0.3
Fe_2O_3 (Fe^{3+}) (keV)	7.1099	7.1171	7.1205	7.1287
Chemical shift† (eV)		9.4	5.7	2.4
Deviation between Fe^{3+} and Fe^{2+} (eV)	2.3	5.6	6.1	5.2

† The chemical shift is estimated from the deviation from the XANES curve of iron metal foil.

chemical shifts of, in ascending order of energy, 3.8, 6.7, 8.1 and 9.4 eV, respectively. The peak tops of the main-edge spectra exhibit deviations of -2.8 , -0.1 , 0.3 and 2.4 eV from that of iron metal foil, respectively.

4. Valence-contrast approach

The first step in determining the valence distribution of Fe^{2+} and Fe^{3+} is to estimate experimentally based atomic scattering factors for valence ions for crystal-structure analyses (VDC method) (Sasaki, 1995). In kinematical diffraction theory, the X-ray Bragg intensity I_{hkl} for the hkl reflection is proportional to the square of the crystal-structure factor F_{hkl} :

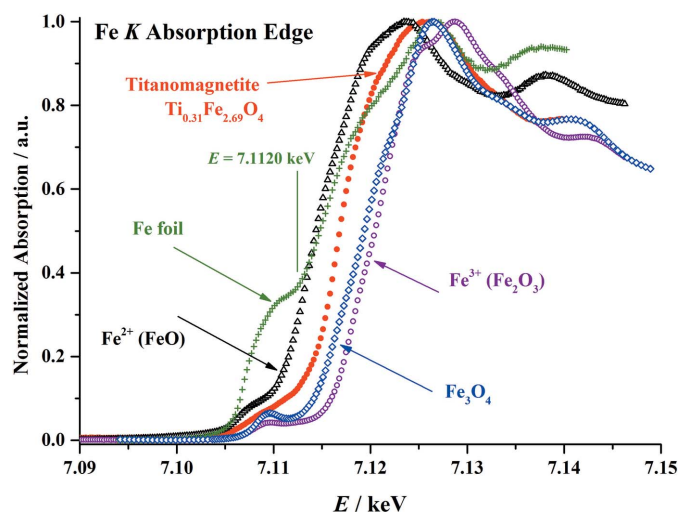


Figure 2 XANES spectra of titanomagnetite (red solid circles), iron foil (green crosses), FeO (black open triangles), Fe_3O_4 (blue open rectangles) and Fe_2O_3 (purple open circles) near the Fe K absorption edge.

$$I_{hkl} \propto |F_{hkl}|^2, \quad (1)$$

$$F_{hkl} = \sum_j f_j \exp[2\pi i(hx_j + ky_j + lz_j)] \exp(-W_j), \quad (2)$$

where the summation j is over all atoms in a unit cell and f , (x, y, z) and W are the atomic scattering factor, fractional coordinates and Debye–Waller factor, respectively. The effect of resonant scattering becomes dominant at photon energy E of the absorption edge. Then, the atomic scattering factor is redefined as

$$f(s, E) = f_0(s) + f'(E) + if''(E), \quad (3)$$

where $f_0(s)$, $f'(E)$ and $f''(E)$ are the Thomson elastic scattering term and the real and imaginary parts of the anomalous scattering factor, respectively, and $s = \sin \theta / \lambda$ with Bragg angle θ and wavelength λ . The anomalous scattering factor was selected here to increase the difference between two types of cation in different valence states. The term $f''(E)$ is related to the absorption coefficient $\mu(E)$ through the optical theorem as forward scattering ($s = 0$),

$$\mu(E) = (4\pi N h e^2 / m E) f''(E'). \quad (4)$$

Using the Kramers–Krönig transform, $f'(E)$ is given from the dispersion relations as

$$f'(E) = (2/\pi) P \int [E' f''(E') / (E^2 - E'^2)] dE', \quad (5)$$

where the integration is from zero to infinity, and P indicates the principal value of the integral at the singularity in the algorithms of the *DIFFKK* program (Cross *et al.*, 1998) used in this study. According to equations (4) and (5), $f''(E)$ can be determined from observed values of $\mu(E)$ and connected to $f'(E)$ in the Kramers–Krönig dispersion relation. According to the crystal field theory, the difference of electron stabilization energies between octahedral and tetrahedral sites is small, having values of 0 and 0.07 eV mol⁻¹ for Fe³⁺ and Fe²⁺, respectively (McClure, 1957). Therefore, if the valence of ions is the same regardless of the different surroundings, the same anomalous scattering factors can be applied for the VDC method on the octahedral and tetrahedral coordination. There is also a report that the shift of the absorption edge is similar for both tetrahedral and octahedral Fe atoms in magnetite, based on the anomalous scattering factors extracted from experimental diffraction spectra of the 220 and 222 reflections [see Fig. 10 by Subías *et al.* (2012)].

The experimentally based $f'(E)$ values were obtained from equation (5) using the *DIFFKK* program (Cross *et al.*, 1998), where $f'(E)$ was estimated from the free atom calculations far from resonance (Cromer & Liberman, 1970), and the values in the reported table were used for unobserved $\mu(E)$ data away from the edge (Sasaki, 1990). In order to simplify the discussion, it is assumed that oxygen is divalent. Fig. 3 shows $f'(E)$ curves for Fe²⁺ and Fe³⁺, obtained from the FeO and Fe₂O₃ absorption data, respectively, where a sharp negative peak in each $f'(E)$ curve exists with the chemical shift. It should be noted that the $f'(E)$ difference due to a chemical shift becomes dominant in the vicinity of the lower-energy side of

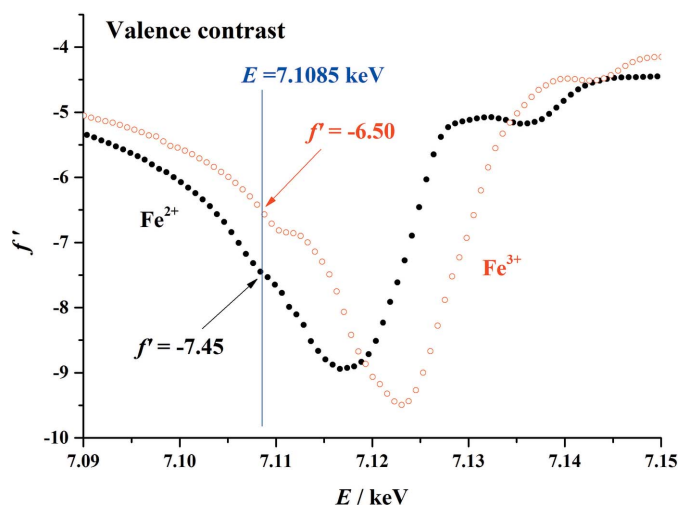


Figure 3 Valence contrast of Fe ions in f' , where the energy dependences of f' for FeO (black solid circle) and Fe₂O₃ (purple open circle) were determined by the Kramers–Krönig transform of the XANES data.

the absorption edge. The X-ray energy in the region is also suitable for diffraction experiments based on weak absorption (Sasaki, 1995). In this study a typical wavelength of $\lambda = 1.7441 \text{ \AA}$ ($E = 7.1085 \text{ keV}$) was selected for the VDC analyses, where the $f'(E)$ values are -7.45 and -6.50 for Fe²⁺ and Fe³⁺, respectively. A large difference of 0.95 in $f'(E)$ promises successful structure analyses that can distinguish Fe²⁺ and Fe³⁺. The value of $f'(E)$ for Fe³⁺ of -6.206 at $E = 7.1082 \text{ keV}$ was obtained from nickel ferrite NiFe₂O₄ of the same spinel structure (Okube *et al.*, 2012), and it is sufficiently close to the value for Fe₂O₃ to be reasonable. Total atomic scattering factors $f(s, E)$ for Fe²⁺, Fe³⁺ and Ti⁴⁺ are shown in Fig. 4, where the large differences between the three cations ensure distinguishability.

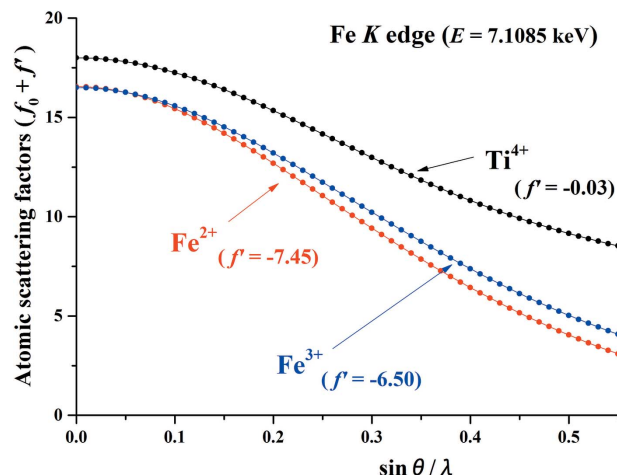
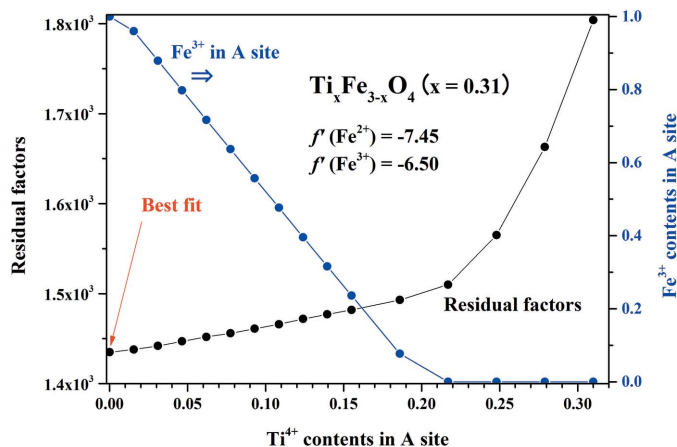


Figure 4 Atomic scattering factors $f_0 + f'$ for Fe²⁺, Fe³⁺ and Ti⁴⁺ against $\sin \theta / \lambda$ for X-ray experiments at the Fe *K* pre-edge ($E = 7.1085 \text{ keV}$). Since the cubic spinel structure has a center at the origin, the crystal structure factor lies near the real axis of the complex plane (see Table 2). Then, atomic scattering factors in this plot may be approximately expressed as $f_0 + f'$.


Figure 5

Variation in the converged residual factors as a function of Ti^{4+} population in the tetrahedral A site. Black solid circles indicate the residual factors. Fe^{3+} contents in A sites are shown in blue solid circles. The red arrow indicates the best fit of our site occupancy refinement.

Charge neutrality in a unit cell was assumed during the site-occupancy refinements, with all titanium ions defined as Ti^{4+} , and A and B sites assumed to be fully occupied by atoms. In the refinements, the occupancy parameters of Fe^{2+} and Ti^{4+} in the tetrahedral A site were varied, while the other parameters were constrained for Fe^{3+} on the A sites and all ions on the B site. The Ti^{4+} content of the A sites was used as an input parameter that was changed in each site-occupancy refinement step. Fig. 5 shows the variation in the residual factor for different Ti^{4+} and Fe^{3+} contents. The A site is fully occupied by Fe^{3+} , and the titanomagnetite presents as $[\text{Fe}_{1.00}^{3+}]^A[\text{Fe}_{0.38}^{3+}\text{Fe}_{1.31}^{2+}\text{Ti}_{0.31}^{4+}]^B$ with a chemical formula of $\text{Ti}_{0.31}\text{Fe}_{2.69}\text{O}_4$, where A and B are the tetrahedral A and octahedral B sites, respectively. In order to check the reliability concerning the convergence of refinements in Fig. 5, further refinement was carried out to remove the constraint on chemical composition. Then, a multiplicity parameter of Fe^{2+} in the A site converged to be -0.01 (8), suggesting that a minimum of the residual factors locates in close proximity at the left-hand side of Fig. 5 and supporting the full occupation of Fe^{3+} in the A site. The cation distribution investigated so far is consistent with the Néel model in that Fe^{3+} completely fills the tetrahedral site and the remaining cations occupy the octahedral site (Néel, 1955; Chevallier *et al.*, 1955). Fe^{3+} replacement by Ti^{4+} yields a proportional increase in Fe^{2+} within the octahedral B site and is maintained to within at least one-third in the Ti-poor solid solution of titanomagnetite.

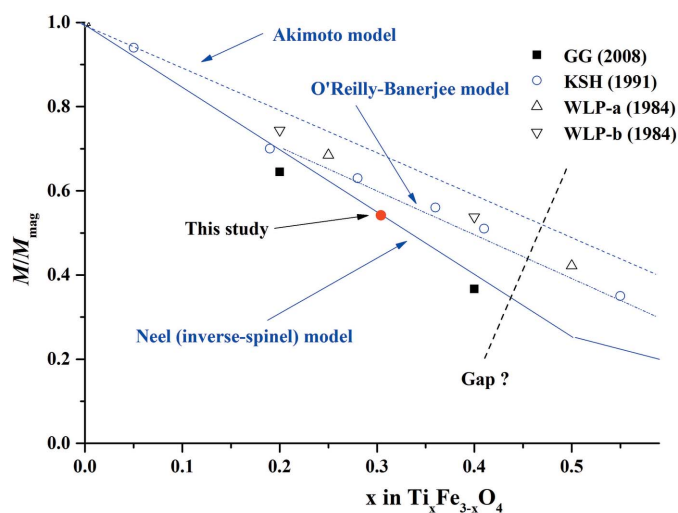
5. Cation distribution and magnetic aspect

The composition of $x = 0.31$ in the $\text{Ti}_x\text{Fe}_{3-x}\text{O}_4$ solid solution corresponds to one end of a miscibility gap in the phase diagram between Fe_3O_4 and TiFe_2O_4 . It may affect the magnetic aspect of titanomagnetite and magnetic measurements. According to the entropy of mixing and thermodynamics of the solid solution, the solvus was suggested to be at or higher than a temperature of $T = 530$ K, although this

temperature is variable depending on the initial composition and exsolution [Fig. 6 of Lilova *et al.* (2012)]. The maximum x value previously reported is 0.42, giving a critical temperature of 873 K (Kawai, 1956).

The distribution of Fe^{2+} and Fe^{3+} between the A and B sites can be calculated based on the observed saturation moments of $4.06\mu_B$ and $5\mu_B$ for Fe^{2+} and Fe^{3+} , respectively (*e.g.* Kakol *et al.*, 1991). However, because of the above assumption, the accuracy of the Fe^{2+} and Fe^{3+} distribution is limited by the sample quality of the magnetic and chemical measurements. In discussions to improve the accuracy, a magnetization ratio normalized with the value for Fe_3O_4 was introduced to compare magnetic moments with the chemical composition. Fig. 6 shows the magnetization ratio *versus* Ti content, where the observed data [GG: Gilder & Le Goff (2008); KSH: Kakol *et al.* (1991); WLP: Wechsler *et al.* (1984)] are plotted together with the calculation ratio of $[\text{Fe}_{1.00}^{3+}]^A[\text{Fe}_{1-2x}^{3+}\text{Fe}_{1+x}^{2+}\text{Ti}_x^{4+}]^B\text{O}_4$ ($x = 0.31$). The magnetization ratio estimated from the site occupancy obtained in this study is close to that reported by Gilder & Le Goff (2008), which is a high-temperature product produced by the floating-zone method, with reorientation of the domain walls conducted with anhysteretic remnant magnetization.

According to previous studies (Blasse, 1964; Forster & Hall, 1965; Fujino, 1974), titanium as Ti^{4+} exclusively occupies the octahedral sites of titanomagnetite. As to the distribution of Fe^{2+} and Fe^{3+} between the A and B sites, three different models exist, as mentioned in the *Introduction*. Magnetic moments calculated using these models are plotted in Fig. 6 using dotted, solid and two dot chain lines, respectively. The experimental values are also shown using solid squares (GG), open circles (KSH) and triangles (WLP), where GG is close to the Néel model, while KSH and WLP have a linear relation close to but of different slope from the O'Reilly–Banerjee


Figure 6

Magnetization ratios for titanomagnetite normalized on the end-member value of Fe_3O_4 . The magnetization ratios obtained from the magnetization measurements are indicated as GG (Gilder & Le Goff, 2008), KSH (Kakol *et al.*, 1991), WLP-a and WLP-b (Wechsler *et al.*, 1984), shown in the figure as filled squares, open circles, open down-triangles (magnetic data) and open up-triangles (neutron diffraction data), respectively.

model. A theoretical treatment of cation distribution for the Néel model is based on the concept that Fe^{3+} prefers the tetrahedral *A* site in thermal activation energy, where the equilibrium as a function of temperature is in agreement with the compositional variation of the magnetic moment and differs from the results for single crystals (Stephenson, 1969). Analysis of the saturation magnetization data suggests that the cation distribution in the titanomagnetite solid solution series is temperature dependent (Bleil, 1976). Specifically, for higher crystal growth temperatures, the magnetic susceptibility becomes closer to either the Akimoto or O'Reilly–Banerjee model. The KSH and WLP data in Fig. 6 are acceptable on a straight line of the O'Reilly–Banerjee model because the temperature of crystal formation was 1373 K or more.

In contrast, the cation distribution obtained in this study is in line with the Néel model, providing the conclusion that the crystal-formation temperature is rather low in comparison with the KSH and WLP data. Perfect occupation of Fe^{3+} in a single *A* site might have taken place due to natural slow cooling and geological time. However, it is uncertain whether the sample has reached its most ordered state without further knowledge of the diffusion coefficient. The confusion among the previous studies on titanomagnetite may be due to the different thermal history. It is considered from this study that the ordering scheme of titanomagnetite is analogous to that of magnetite, having a similar trend to the temperature dependence of magnetocrystalline anisotropy by torque measurements (Syono & Ishikawa, 1963). As a possibility other than the thermal history, the relatively low magnetic moments previously observed could be also related to domains and domain walls caused by the discrepancy with Ti-doping which are formed to align neighboring regions magnetized anti-parallel to one another, where the magnitude of the magnetic moments can change gradually to depend on the orientation of the neighboring moments in a realistic crystal. In addition, the covalent contribution to the chemical bonding makes the magnetic moments lower than those expected for ideal Fe^{2+} and Fe^{3+} . An increase in the tetrahedral Fe^{2+} content leads to a high coercive force with enhanced magnetostriction. Given that the intermediate composition has characteristic broad spectra both in X-ray diffraction and Mössbauer spectroscopy, local environments due to the random arrangements are suggested for Fe^{2+} and Ti^{4+} in the *B* site (Banerjee *et al.*, 1967). One study has reported that net moments derived from neutron powder diffraction are 5–10% lower than saturation magnetizations as determined from magnetometer measurements (Wechsler *et al.*, 1984).

6. Diffractometry near absorption edges

In the case of protein crystals with a relatively low content of resonant scattering elements, the influences of absorbed or fluorescent X-rays are not a serious problem even in diffraction experiments in the vicinity of the absorption edge. On the other hand, in the case of inorganic or metallic crystals, where the proportion of transition-metal element may be up to several tens of percent, the fluorescent X-ray background

intensity and air scattering cannot be ignored. Generally, the use of a two-dimensional detector makes it difficult to handle the effect by fluorescent and air-scattered X-rays because of the technical limitation to set slits in front of the detector. Therefore, the use of a four-circle diffractometer is re-recognized here by combining circularly polarized X-rays and a scintillation counter with receiving slits.

Since conventional synchrotron radiation is linearly polarized in the horizontal plane, the detector axis 2θ of the diffractometer is generally vertical. However, when the circular polarization is introduced by the phase retarder described in §2, a sufficient incident intensity can be obtained in horizontal-type diffractometry on the polarization effect. This implies the possibility of using a commercial four-circle diffractometer for synchrotron radiation research, having a horizontal 2θ axis and a polarization factor equal to that of unpolarized beam. The transmittance of the diamond crystal as phase retarder is about 40% near the Fe *K*-edge [Fig. 3(b) of Matsumoto *et al.* (2000)].

Since the use of receiving slits has the advantage of reducing experimental noise, a Rigaku AFC-5R four-circle diffractometer, with a χ circle of diameter 190 mm and a sample to receiving slit distance of 258 mm, was installed on beamline BL-6C, where circularly polarized X-rays are available (Fig. 7). The small circle guarantees high precision in intersection accuracy of four circles, even though the latest single-crystal diffractometer no longer requires such accuracy due to the development of two-dimensional detectors. The AFC-5R diffractometer can be controlled sufficiently even now by the original software for determining and refining the orientation matrix and the data collection procedure. A set of receiving slits consists of both vertical and horizontal apertures in front of the scintillation counter. Even when a larger pair of slits is used as the maximum aperture of 1° (4.5 mm \times 4.5 mm)

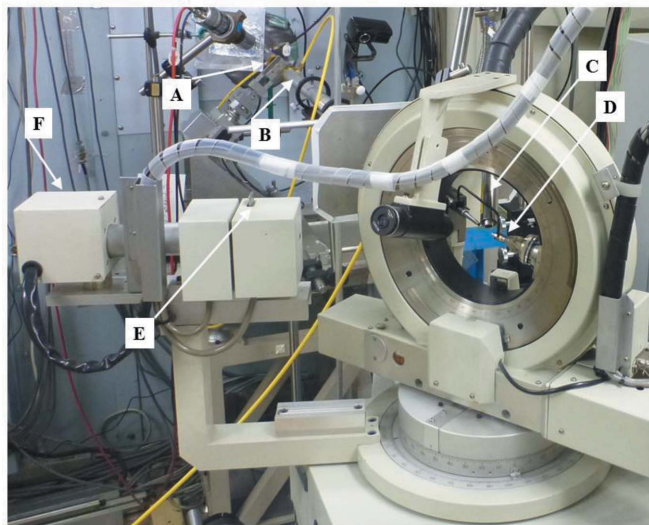


Figure 7
Four-circle diffractometer and phase retarder installed in the experimental hutch of BL-6C at the Photon Factory. A: phase retarder. B: He pass. C: nozzle of low-temperature equipment (not used in this study). D: sample on goniometer head. E: receiving slits. F: scintillation detector.

Table 2

Integrated peak and background intensities in counts for some strong and weak Bragg reflections of titanomagnetite.

<i>hkl</i>	Peak intensity (counts)	Background (counts)				Scattering angle 2θ ($^\circ$)	Crystal structure factor F_{calc}
		1†	2†	3†	4†		
400	139575	2298	24	430	719	49.17	$522.43 + i22.33$
800	54102	2280	24	759	381	112.62	$373.44 + i26.80$
440	154010	5480	57	408	2332	72.06	$633.46 + i28.69$
311	108751	3030	32	489	1026	40.36	$-349.29 - i14.43$
511	47399	1444	15	340	382	65.42	$276.32 + i14.15$
444	31831	1102	11	310	241	92.21	$274.21 + i20.89$
200	1386	1312	14	349	307	24.01	0
600	354	356	4	90	88	77.22	0
822	2863	544	6	182	90	123.89	$-66.98 - i3.22$
733	444	382	4	101	90	116.71	$-1.60 + i7.66$
Measuring time (s)	96	96	1	24	24		

† 1: Normalization is the same as the peak-integration time of 96 s. 2: Counts s^{-1} . 3 and 4: Measurements at 0.4° lower and higher positions in ω , respectively.

without analyzer, the background intensity was suppressed to around 10 counts s^{-1} in the experiment with titanomagnetite (Table 2). This is within a level that the crystal structure of titanomagnetite can be analyzed sufficiently and accurately even when the intensity measurement was performed in the presence of the fluorescence of Ti atoms. The consistent results on the site occupancy obtained from the VDC method strongly support the advantage of using the four-circle diffractometer. Thus, it can be concluded that our diffraction experiment at the absorption edge provides sufficient accuracy even in the air rather than in a vacuum.

The diffractometer was originally designed and installed for experiments of resonant X-ray magnetic scattering (Kaneko *et al.*, 2010; Sasaki *et al.*, 2017). Since the phase retarder needs parallel beam and the focusing mirror pre-installed on beamline BL-6C is located in front of the retarder, a special mirror of a graded parabolic W/Si multilayer (length = 40 mm, period of multilayer = $32.90 \simeq 40.29 \text{ \AA}$, parabolic parameter = 0.11838, focal length = 100 mm, reflectivity $\simeq 65\%$) can be optionally placed at a distance of 155 mm in front of the center of the diffractometer (Sasaki *et al.*, 2013).

7. Conclusion

A VDC study with synchrotron X-ray diffraction confirmed that Fe^{3+} in natural titanomagnetite prefers the tetrahedral *A* site in the AB_2O_4 structure, while all of Fe^{2+} and Ti^{4+} occupy the octahedral *B* site. The site occupancy can be schematically written as $[\text{Fe}_{1.00}^{3+}]^A [\text{Fe}_{0.38}^{3+} \text{Fe}_{1.31}^{2+} \text{Ti}_{0.31}^{4+}]^B$. It was found that the cation distribution coincides with the Néel model, providing the conclusion that the crystal formed at a rather low temperature and the magnetic structure can be discussed based on that of magnetite. It was found from a comparison with synthetic samples of the similar composition that the crystal-formation temperature of the natural titanomagnetite

is lower than the synthesis temperature in the published studies and exhibits perfect ordering of the cation distribution.

It was shown by application of the VDC techniques that the following features can be realized in the diffraction experiments near the absorption edges. (1) Chemical shifts of XANES spectra are useful to determine the valence of Fe ions among different iron oxides. (2) Experimental values of anomalous scattering factors can be successfully converted from the absorption data by using the *DIFFKK* software (Cross *et al.*, 1998). (3) The circular polarization introduced by the phase retarder increases freedom in diffractometry. (4) Since a small and compact four-circle diffractometer has

good crossing accuracy, the combination of circularly polarized X-rays and horizontal-type diffractometer has the advantage of increasing the experimental accuracy. (5) The use of receiving slits in front of the scintillation counter of the four-circle diffractometer can reduce experimental noise, which appears due to the fluorescence and air scattering of X-rays.

Acknowledgements

The authors are grateful to Professor H. Kawata and Mr H. Ohta of the Photon Factory and to Dr H. Arima of Tohoku University for their support in our experiments. This study was performed at BL-6C and partly BL-10A under the auspices of the Photon Factory (PAC Nos. 2016G097 and 2016G011).

Funding information

The following funding is acknowledged: JSPS KAKENHI (grant No. 15H03747).

References

- Akimoto, S. (1954). *J. Geomagn. Geoelec.* **6**, 1–14.
- Akimoto, S., Katsura, T. & Yoshida, M. J. (1957). *J. Geomagn. Geoelec.* **9**, 165–178.
- Banerjee, S. K., O'Reilly, W., Gibb, T. C. & Greenwood, N. N. (1967). *J. Phys. Chem. Solids*, **28**, 1323–1335.
- Barth, T. F. & Posnjak, E. (1932). *Z. Kristallogr.* **482**, 325–341.
- Beale, T. A. W., Beutier, G., Bland, S. R., Bombardi, A., Bouchenoire, O., Bunäu, O., Di Matteo, S., Fernández-Rodríguez, J., Hamann-Borrero, J. E., Herrero-Martín, J., Jacques, V. L. R., Johnson, R. D., Juhin, A., Matsumura, T., Mazzoli, C., Mulders, A. M., Nakao, H., Okamoto, J., Partzsch, S., Princep, A. J., Scagnoli, V., Stempfer, J., Vecchini, C., Wakabayashi, Y., Walker, H. C., Wermeille, D. & Yamasaki, Y. (2012). *Eur. Phys. J. Spec. Top.* **208**, 89–98.
- Becker, P. J. & Coppens, P. (1974). *Acta Cryst.* **A30**, 129–147.
- Blasse, G. (1964). *Philips Res. Rep. Suppl.* **3**, 1–139.
- Bleil, U. (1971). *Z. Geophys.* **37**, 305–319.
- Bleil, U. (1976). *Pure Appl. Geophys.* **114**, 165–175.
- Bosi, F., Hålenius, U. & Skogby, H. (2009). *Am. Mineral.* **94**, 181–189.
- Bragg, W. H. (1915). *Philos. Mag.* **30**, 305–315.

- Chevallier, R., Bolfà, J. & Mathieu, S. (1955). *Bull. Soc. Fr. Miner. Cristallogr.* **78**, 307–346.
- Cromer, D. T. & Liberman, D. (1970). *J. Chem. Phys.* **53**, 1891–1898.
- Cross, J. O., Newville, M., Rehr, J. J., Sorensen, L. B., Bouldin, C. E., Watson, G., Gouder, T., Lander, G. H. & Bell, M. I. (1998). *Phys. Rev. B*, **58**, 11215–11225.
- Forster, R. H. & Hall, E. O. (1965). *Acta Cryst.* **18**, 857–862.
- Fujino, K. (1974). *Miner. J.* **7**, 472–488.
- Gilder, S. A. & Le Goff, M. (2008). *Geophys. Res. Lett.* **35**, L10302.
- Grenier, S., Toader, A., Lorenzo, J. E., Joly, Y., Grenier, B., Ravy, S., Regnault, L. P., Renevier, H., Henry, J. Y., Jegoudez, J. & Revcolevschi, A. (2002). *Phys. Rev. B*, **65**, 180101.
- Hamdeh, H. H., Barghout, K., Ho, J. C., Shand, P. M. & Miller, L. L. (1999). *J. Magn. Magn. Mater.* **191**, 72–78.
- Hirano, H., Izumi, K., Ishikawa, T., Annaka, S. & Kikuta, S. (1991). *Jpn. J. Appl. Phys.* **30**, L407–L410.
- Iizumi, M., Koetzle, T. F., Shirane, G., Chikazumi, S., Matsui, M. & Todo, S. (1982). *Acta Cryst.* **B38**, 2121–2133.
- Ishikawa, Y. (1967). *Phys. Lett. A*, **24**, 725–727.
- Óakol, Z., Sabol, J. & Honig, J. M. (1991). *Phys. Rev. B*, **43**, 649–654.
- Kaneko, Y., Okube, M., Sasaki, S., Garrett, R., Gentle, I., Nugent, K. & Wilkins, S. (2010). *AIP Conf. Proc.* **1234**, 883–886.
- Kawai, N. (1956). *Proc. Jpn Acad.* **32**, 46–68.
- Lilova, K. I., Pearce, C. I., Gorski, C., Rosso, K. M. & Navrotsky, A. (2012). *Am. Mineral.* **97**, 1330–1338.
- McClure, D. S. (1957). *J. Phys. Chem. Solids*, **3**, 311–317.
- Matsumoto, K., Saito, F., Toyoda, T., Ohkubo, K., Yamawaki, K., Mori, T., Hirano, K., Tanaka, M. & Sasaki, S. (2000). *Jpn. J. Appl. Phys.* **39**, 6089–6093.
- Nakao, H., Kiyoto, K., Kodama, S., Bizen, D., Matsumura, T., Iwasa, K., Murakami, Y. & Ochiai, A. (2006). *AIP Conf. Proc.* **850**, 1175–1176.
- Néel, L. (1955). *Adv. Phys.* **4**, 191–243.
- Nishikawa, S. (1915). *Proc. Tokyo Math. Phys. Soc.* **8**, 199–209.
- Ohara, H., Mizobuchi, T., Matsumoto, K. & Sasaki, S. (2000). *Proceedings of the Eighth International Conference on Ferrites (ICF-8)*, 18–21 September 2000, Kyoto, Japan, pp. 223–225.
- Ohara, H., Sasaki, S., Konoike, Y., Toyoda, T., Yamawaki, K. & Tanaka, M. (2004). *Physica B*, **350**, 353–365.
- Okita, A., Saito, F., Sasaki, S., Toyoda, T. & Koinuma, H. (1998). *Jpn. J. Appl. Phys.* **37**, 3441–3445.
- Okube, M. & Sasaki, S. (2014). *J. Appl. Cryst.* **47**, 1387–1394.
- Okube, M., Yasue, T. & Sasaki, S. (2012). *J. Synchrotron Rad.* **19**, 759–767.
- Ôno, K., Chandler, L. & Ito, A. (1968). *J. Phys. Soc. Jpn.* **25**, 174–176.
- O'Reilly, W. & Banerjee, S. K. (1965). *Phys. Lett.* **17**, 237–238.
- Palancher, H., Hodeau, J.-L., Pichon, C., Bélar, J.-F., Lynch, J., Rebours, B. & Rodriguez-Carvajal, J. (2005). *Angew. Chem. Int. Ed.* **44**, 1725–1729.
- Pearce, C. I., Henderson, C. M. B., Telling, N. D., Patrick, R. A. D., Charnock, J. M., Coker, V. S., Arenholz, E., Tuna, F. & van der Laan, G. (2010). *Am. Mineral.* **95**, 425–439.
- Sakurai, S., Sasaki, S., Okube, M., Ohara, H. & Toyoda, T. (2008). *Physica B*, **403**, 3589–3595.
- Samuelsen, J., Bleeker, E. J., Dobrzynski, L. & Riste, T. (1968). *J. Appl. Phys.* **39**, 1114–1115.
- Sasaki, S. (1987). *KEK Internal Rep.* **87-2**, 1–175.
- Sasaki, S. (1990). *KEK Rep.* **90-16**, 1–143.
- Sasaki, S. (1995). *Rev. Sci. Instrum.* **66**, 1573–1576.
- Sasaki, S., Okube, M. & Fujinawa, G. (2013). *The 12th Conference of the Asian Crystallographic Association (AsCA2013)*, HKUST, Hong Kong, 7–13 December 2013. P081.
- Sasaki, Y., Okube, M. & Sasaki, S. (2017). *Acta Cryst.* **A73**, 257–270.
- Sasaki, S., Toyoda, T., Yamawaki, K. & Ohkubo, K. (1998). *J. Synchrotron Rad.* **5**, 920–922.
- Screaton, G. R. (1960). Editor. *Dispersion Relations*. Edinburgh: Oliver and Boyd.
- Stephenson, A. (1969). *Geophys. J. Int.* **18**, 199–210.
- Subías, G., García, J., Blasco, J., Herrero-Martín, J., Sánchez, M. C., Orna, J. & Morellón, L. (2012). *J. Synchrotron Rad.* **19**, 159–173.
- Syono, Y. & Ishikawa, Y. (1963). *J. Phys. Soc. Jpn.* **18**, 1230–1231.
- Thompson, A. C., Attwood, D. T., Gullikson, E. M., Howells, M. R., Kortright, J. B., Robinson, A. L. & Underwood, J. H. (2001). *X-ray Data Booklet*, revision 2, pp. 1–8, LBNL/PUB-490. Lawrence Berkeley National Laboratory, Berkeley, CA, USA.
- Toyoda, T., Sasaki, S. & Tanaka, M. (1997). *Jpn. J. Appl. Phys.* **36**, 2247–2252.
- Toyoda, T., Sasaki, S. & Tanaka, M. (1999). *Am. Mineral.* **84**, 294–298.
- Tsukimura, K., Sasaki, S. & Kimizuka, N. (1997). *Jpn. J. Appl. Phys.* **36**, 3609–3612.
- Verwey, E. J. W. & de Boer, J. H. (1936). *Recl Trav. Chim. Pays Bas*, **55**, 531–540.
- Verwey, E. J. W. & Haayman, P. W. (1941). *Physica*, **8**, 979–987.
- Verwey, E. J. W., Haayman, P. W. & Romeijn, F. C. (1947). *J. Chem. Phys.* **15**, 181–187.
- Wechsler, B. A., Lindsey, D. H. & Prewitt, C. T. (1984). *Am. Mineral.* **69**, 754–770.
- Wilkinson, A. P. & Cheetham, A. K. (1992). *J. Appl. Cryst.* **25**, 654–657.
- Yakel, H. L. (1980). *J. Phys. Chem. Solids*, **41**, 1097–1104.
- Yamada, T., Suzuki, K. & Chikazumi, S. (1968). *Appl. Phys. Lett.* **13**, 172–174.